RESEARCH ARTICLE | DECEMBER 05 2023

Passive flow control for the E423 airfoil utilizing an equilateral triangular trip

Salman Rahmani ; Z. J. Wang

Physics of Fluids 35, 124105 (2023)
https://doi.org/10.1063/5.0174284
CHORUS

Physics of Fluids ARTICLE pubs.aip.org/aip/pof

Passive flow control for the E423 airfoil utilizing an equilateral triangular trip

Cite as: Phys. Fluids **35**, 124105 (2023); doi: 10.1063/5.0174284
Submitted: 29 August 2023 · Accepted: 14 November 2023 ·
Published Online: 5 December 2023

Salman Rahmani[a] and Z. J. Wang

AFFILIATIONS

Department of Aerospace Engineering, The University of Kansas, Lawrence 66045, USA

[a]Author to whom correspondence should be addressed: salmanr@ku.edu

ABSTRACT

A passive flow control technique of utilizing an equilateral triangular trip close to the leading edge was developed and tested for a micro-scale Eppler E423 airfoil at a Reynolds number based on the chord of 40 000. The analysis was carried out via high-order wall-resolved large eddy simulation using the computational solver HpMusic. Angles of attack of 5° and 20° were tested. It was shown that at an angle of attack of 5°, the trip height of two times the local boundary layer thickness outperformed existing passive flow control techniques from the literature by almost a factor of five in terms of the lift-to-drag ratio. To understand the underlying physics which allowed the trip to provide this very significant performance benefit, metrics such as pressure coefficient profiles, oil flows, iso-surfaces of Q-criteria, and leading-edge flow behavior were examined. It was found that this trip configuration simultaneously removed the flow separation regions on both the suction and pressure sides of the wing.

NOMENCLATURE

C_D	Drag coefficient
$\bar{C}_D$	Temporally averaged drag coefficient
c	Chord length
E	Total energy
$\vec{F}$	Flux vector
M	Mach number
$\vec{m}$	Vector of momentum components
P	Static pressure
P_t	Total pressure
p	Spatial solution polynomial order
Q	Vector of conservative flow variables
Re_c	Reynold's number based on chord
T_t	Total temperature
T_u	Convective time unit
t	Time
u_∞	Freestream velocity
x	Location in streamwise direction
x^+_{equiv}	Surface mesh resolution in streamwise direction
y	Location in wall-normal direction
y^+_{equiv}	Surface mesh resolution in wall-normal direction
z	Location in spanwise direction
z^+_{equiv}	Surface mesh resolution in spanwise direction
α	Angle of attack
δ	Boundary layer height
Δx_{max}	Largest surface element size in streamwise direction
Δy_{max}	Largest surface element size in wall-normal direction
Δz_{max}	Largest surface element size in spanwise direction
ρ	Density

I. INTRODUCTION

The ability to achieve controlled, sustainable flight for drones at increasingly smaller scales continues to be an area of active research. Notable progress has been made in the following drone classes: super-heavy, large, medium, and small.[1–10] However, drones weighing between 2 kg and 250 g, known as micro-air vehicles (MAVs), and drones weighing under 250 g, also known as nano-air vehicles (NAVs), suffer from high sensitivity to atmospheric turbulence, low-energy boundary layers, and lack of on-board space for propulsive components.[11–13] These factors culminate to make MAVs and NAVs susceptible to low flight endurance and loss of control. As a result, a primary focus of recent fixed-wing MAV and NAV research has been directed toward stability and flow control.[14–16] One suitable approach to enhance fixed-wing aerodynamic efficiency, primarily at low Reynolds numbers, is the use of flow tripping devices. The goal of the flow tripping device is to force the flow into a turbulent state so that it is more energetic and remains attached to the control surface.[17]

Although there is a consensus that tripping devices do, indeed, preserve flow attachment through this process, answers regarding the optimal trip location and geometry have been established only on a case-by-case basis. For example, Sreejith and Sathyabhama[18] computationally and experimentally evaluated the effectiveness of boundary layer trips (BLTs) on an Eppler E216 airfoil at a Reynolds number of 100 000. Their results showed that for the optimal trip configuration, the flow separation along the suction side of the airfoil was substantially mitigated and the lift-to-drag ratio improved by 34.6%. This work was continued[19] to include two different trip locations: 10% of chord and 17% of chord. After testing a variety of trip heights ranging from 0.3 to 1 mm, they concluded that the lift-to-drag ratio can be improved by 21.62%. Because their results showed such drastic improvement of tripped airfoils over un-tripped airfoils, a third work studying the effects of different trip geometries[20] was produced. In it, they showed that an isosceles-triangle-shaped BLT produced better results over its right-angled-triangular (RAT) and rectangular trip (RT) counterparts. In addition to the previously mentioned triangular trips, one particular BLT device that has gained prominence is vortex generators (VGs). By creating small vortexes that span the chordline of the control surface, VGs have shown to successfully sustain flow attachment to control surfaces by energizing the flow. This has led to several studies analyzing VGs in different configurations.[21,22] Li *et al.*[21] found that using the optimal VG configuration on the DU93-W-210 airfoil, the lift-to-drag ratio was increased by 48.7%, the drag was lowered by 84.9%, and the stall angle was increased by 10° when operated at a Reynolds number of 1×10^6. Similarly, Seshagiri *et al.*[22] experimentally studied the effects of both static and oscillating VGs on a NASA LS(1)-0417GA(W)-1 operating at Reynolds numbers of 80 000 and 160 000. After testing six static VG configurations and one oscillatory VG configuration, their data suggest that although the oscillating VGs had no appreciable effects, the static VGs increased the maximum lift coefficient by 25%. They concluded that this increase in aerodynamic performance was due to the ability of the VGs to reduce the extent of the laminar separation bubble (LSB). Because MAVs require as much lift as possible, high-lift airfoils, such as the Eppler E423,[23] are used typically as the baseline in flight efficiency research. This airfoil has been the subject of several flight efficiency optimization studies at low to moderate Reynolds numbers. In addition to testing a NACA-0012 and USA-28, Allemand and Altman[24] experimentally studied the effects of placing artificial self-deployable flaps on the suction surface of an Eppler E423 airfoil. The intent was to improve the post-stall wing lift performance by having the flaps act as a passive boundary layer flow control mechanism. They found that at a Reynolds number of 200 000, the post-stall lift performance was increased by 15% for the E423 and by 5%–30% for the NACA-0012 and USA-28. They conclude by stating that although they were able to increase the performance of each of the airfoils on a case-by-case basis, no universal flap setting was discovered. Concerning low Reynolds numbers, the work conducted by Bakhtian and Jones[25,26] aimed to enhance the flight characteristics of the E423 airfoil by introducing leading edge flaps similar to those found on Mallards. After running experiments on Reynolds numbers ranging from 40 000 to 140 000, Bakhtian[25] found that the leading-edge flap substantially enhanced the airfoil's performance by augmenting the lift and limiting the drag at certain incidences. Additionally, they concluded that the leading-edge flap acted as a transition device which prevented the formation of separation bubbles. This work was continued by Jones[26] with the inclusion of testing leading edge wires and surface-mounted trips as an additional BLT device. After testing a variety of modified and unmodified E423 airfoils within a Reynolds number range of 40 000–120 000 at various angles of attack (AoAs), the authors found that the leading-edge flap successfully acts as a transition trip by introducing disturbances into the flow which propagate over the upper surface of the wing and prevent LSB formations at high AoAs. Furthermore, they concluded that shallower flap deployment angles become effective at lower AoAs and that leading edge flaps generally outperformed surface-mounted trips. Although a substantial amount of research has been conducted to modify existing airfoil designs to optimize flight efficiency at MAV scales, some recent studies have sought to design entirely new types of airfoils. Di Luca *et al.*[27] presented a new type of airfoil called the Separated Flow Wing (SFW), and performance metrics are compared against an unmodified Eppler E423 airfoil. It was found that at a Reynolds number of 40 000, the SFW is much less sensitive to free-stream turbulence levels over a wide range of AoAs when compared to the E423. This new wing design was then implemented on a 104 g fixed-wing drone and tested. The results indicated that the maximum flight time of the drone with the SFW wing geometry is estimated to be 170 min, almost four times higher than existing fixed-wing drones. A companion paper[28] found that at Reynolds numbers of 20 000 and 10 000, the lift generation of the SFW is within 13% of the results shown for Reynolds number 40 000 when external turbulence is introduced. In addition to the works discussed above, recent developments pertaining to active flow control have been published.[29,30] Although the following works do not explicitly test their new flow control designs on the E423, their contribution to the field of low Reynold's number flow control is of paramount importance and deserves proper recognition. First, Wang *et al*[29] investigated the leading edge vortex (LEV) of a plunging SD7003 in response to active flow control. The flow control methodology used a combination of leading-edge blowing control and mid-chord suction control. They found that the strength of the LEV can be increased by injecting momentum into the leading-edge shear layer. This momentum injection at the leading edge increased the maximum lift coefficient. The second work, conducted by Tadjfar and Kasmaiee,[30] used machine learning to optimize the performance of a pitching NACA0012 in dynamic stall conditions using a suction controller for a Reynold's number of 135 000. By successfully using machine learning as an aerodynamic optimization technique, the authors found that the optimized blowing jet configuration increased the lift-to-drag ratio by 24 times that of the baseline case. In addition, they were able to show that during validation testing, the machine-learning model successfully predicted the optimal jet placement angle to be within 0.5° of the actual optimized jet angle. The purpose of the present study is to present and assess the physics associated with a novel passive flow control design called the equilateral triangular trip (ETT). The innovation stemming from the ETT is twofold. First, the geometry of the ETT is nothing more than an equilateral triangle. This makes the trips easy to model and manufacture. Second, the ETTs are able to successfully eliminate both the suction side and pressure side separation bubbles for the E423 airfoil at $\alpha = 5°$. This leads to a very significant improvement in lift-to-drag ratio which has not yet been observed in previous literature for this airfoil operating in MAV-scale conditions. This manuscript is organized as follows: In Sec. II, the numerical method for solving the flow equations is illustrated briefly.

In Sec. IV, the simulation setup and results are presented. Concluding remarks are then discussed in Sec. V. Finally, it should be noted that all computational simulations performed for this work were carried out at the high-performance computing (HPC) facilities operated by the Center for Research Computing (CRC) at the University of Kansas. The CRC contains a variety of central processing unit (CPU) and graphics processing unit (GPU) computing resources. For this work, four Nvidia A100 GPUs were used for each simulation. As a result, each simulation took approximately six days of continuous computing to complete.

II. NUMERICAL METHOD

A. Spatial discretization

For this work, the compressible Navier–Stokes equations are solved numerically. The Navier–Stokes equations depict the conservation of mass, momentum, and energy for the fluid medium. Let Q denote the conservative flow variables within a differential volume of space. That is, let Q be the column matrix $[\rho, \vec{m}, E]^T$, with ρ representing mass per unit volume, $\vec{m}$ representing momentum per unit volume, and E representing total energy per unit volume. Let the function $\vec{F}$ denote the flux vector, i.e., the peripheral exchange of fluid over the boundary of the differential volume, both its convective and its dissipative parts.[31] With the defined symbols, the Navier–Stokes equations, written in conservative form, are expressed as

$$\frac{\partial Q}{\partial t} = -\nabla \cdot \vec{F}(Q, \nabla Q). \tag{1}$$

A high-order large eddy simulation (LES) tool called HpMusic[32] is used in the computational study to solve Eq. (1). The tool is based on the flux reconstruction (FR) or correction procedure via reconstruction (CPR) method originally developed in Ref. 33 for hyperbolic partial differential equations. The method is capable of handling mixed unstructured meshes,[34,35] has some recent advancements in terms of highly scalable GPU capability,[36] and has far-field aeroacoustic prediction methods.[37] Many further developments took place, and a review of the method was provided in follow-up works.[38,39] This method not only belongs to discontinuous finite element methods, similar to the discontinuous Galerkin (DG)[40] and spectral difference[41] methods, but also has some unique advantages. For viscous flux involving the gradient of conservative variables, we use the Bassi-Rebay 2 scheme.[42] No sub-grid scale stress models are used. Therefore, the present simulations are called implicit LES (ILES). For under-resolved flow features, we employ an accuracy-preserving limiter to stabilize the simulation.[43]

B. Time integration

For problems with complex geometries, it is very challenging to generate a mesh without any bad elements which may have nearly diminishing cell volumes. If a globally explicit time integration scheme is used, the global time step will be extremely small, making the simulation very expensive. With implicit schemes, the time step can be usually selected based more on the physical requirement. In the present study, we employ an optimized backward difference formula, which is second-order accurate and A-stable (BDF2OPT)[44] and involves four time levels. Compared with the usual second-order backward difference formula (BDF2), BDF2OPT has about half the truncation error with a similar computational cost and needs slightly more storage. The implicit system is then solved with the non-linear block lower-upper symmetric Gauss-Seidel (LU-SGS) approach.[45] In order to mimic an SGS approach, the update equation is solved in forward and backward sweeps according to the natural cell ordering in the mesh until the norm of the unsteady residual is reduced sufficiently, normally by two orders of magnitude.[46] On each element, the linear equation is small and is solved with a direct LU-decomposition algorithm. Therefore, the overall solution method is called the LU-SGS scheme, which has two advantages: (1) Only the block diagonal matrix on each element is stored and the memory requirement is much smaller than a fully implicit scheme; (2) Only one loop is necessary to converge the non-linear unsteady residual.

III. OPERATING CONDITIONS AND TRIP CONFIGURATIONS

The Eppler E423 was chosen for this work due to its design optimization for low Reynolds number flows. The airfoil has a chord length of 0.085 m and was simulated at AoAs of 5° and 20°. These two angles of attack were selected because they represent certain milestones pertaining to airfoil performance. The AoA of 5° was chosen because this is the angle at which the SFW[27] obtains its optimal lift-to-drag ratio. Additionally, the AoA of 20° was chosen because this is the angle that the baseline E423 obtains its maximum lift coefficient.[27] For the aspect ratio, the airfoil within this manuscript has an aspect ratio of 40% which is similar to other LES studies.[47–49] The flow conditions were specified such that the Reynolds number based on the chord is 40 000 and the freestream turbulence intensity was set to zero. A summary of the case parameters is shown in Table I. The domain used throughout the study is representative of the wind tunnel from Brown University.[27] Because both the domain and the airfoil are simple geometries, high-order hexahedral meshes were generated in Pointwise. The height of each equilateral trip was based on the boundary layer height, δ, at AoA 5° for the baseline configuration at 5% chord. The location of the trip for all configurations was specified such that the apex of the trip occurred at 5% chord. This location is similar to other passive flow control studies.[50–52] The trip is extruded in the spanwise direction so that the span of the trip equals the span of the airfoil. The resulting two-dimensional equilateral triangular trip is easy to model and was chosen for its simplicity. Figure 1 displays the various trip configurations at the AoA of 5°. For boundary conditions, the tunnel and airfoil surfaces were specified as no-slip walls and the spanwise boundaries were cyclic/periodic. A total-pressure-total-temperature inlet was used, and the static pressure was fixed at the outlet. A visual depiction of the boundary conditions and the flow domain is shown in Fig. 2.

IV. RESULTS AND DISCUSSION

This section focuses on assessing the performance of the tripped and untripped E423 configurations. The cases for the AoA of 5° will be presented first, followed by the results for the AoA of 20°. All results shown in this document have a spatial polynomial order of three. This is based on previously conducted p-refinement and mesh refinement studies.

TABLE I. Operating conditions for the E423 airfoil.

P_t^{inlet}/P^{outlet}	α (deg)	Re_c	c (m)	M
1.028	5,20	40 000	0.085	0.2

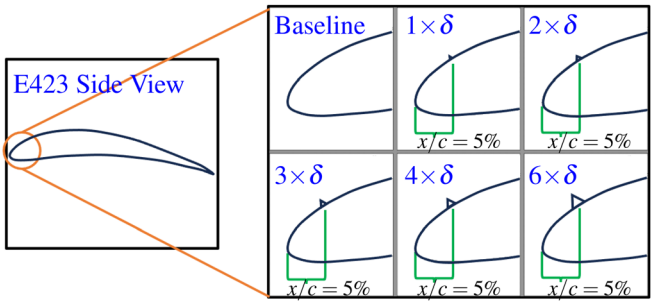

FIG. 1. The E423 geometry and the trip configurations.

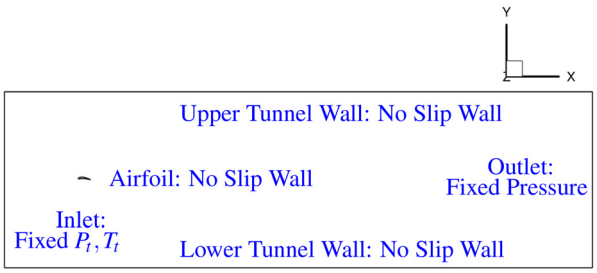

FIG. 2. Flow domain with boundary condition labels.

A. AoA of 5°

The number of elements, degrees of freedom (DOFs), and other relevant mesh metrics for each simulation can be seen in Table II. The height of the first cell along the airfoil, denoted as Δy, was kept constant. The length of the first cell at the leading edge was 0.5% of the chord length. At the location of each trip, the height and length of the first cell was such that the cell became isotropic. After the trip, the streamwise spacing of the elements grew at 25% until reaching the maximum size at the mid-chord location. After the mid-chord location, the streamwise spacing shrank at 1% until reaching the trailing edge, similar to the baseline mesh. The meshes for the $2\times\delta$, $3\times\delta$, and $4\times\delta$ configurations are shown in Fig. 3. With the exception of the mesh around the trip, the mesh is identical to the baseline case, i.e., same spanwise spacing, off-body refinement region of one chord length, and post refinement region growth rate of 50%.

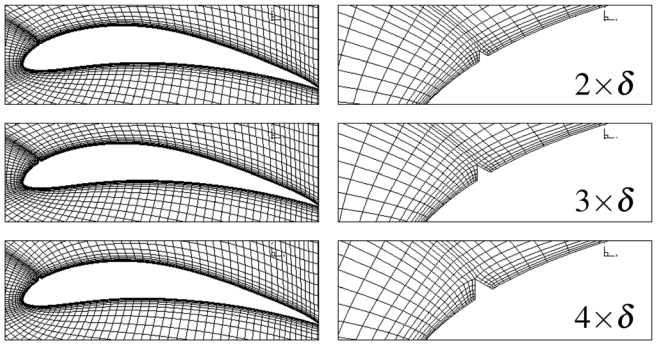

FIG. 3. Tripped E423 meshes for the AoA of 5°.

Each configuration was sampled for eighty convective time units (T_u) after reaching a quasi-steady state where one convective time unit is defined as

$$T_u = \frac{c}{u_\infty}. \tag{2}$$

This metric of eighty convective time units was selected based on previous recommendations[53] and far exceeds the averaging time used by other studies.[54] To ensure that no transient phenomena occurred within the eighty convective time unit sampling period, the time history of the drag coefficient was plotted and is shown in Fig. 4. The lift coefficient (C_L), drag coefficient (C_D), and lift-to-drag ratio (C_L/C_D) for each configuration are shown in Table III. It is shown that the $1\times\delta$ configuration obtains almost the same drag coefficient as the baseline case but simultaneously reduces the measured lift coefficient. This results in a detrimental effect to the lift-to-drag ratio. On the other hand, all ETT configurations which have a trip height greater than one show substantial improvement to all three of the integrated quantities. It is also shown that the C_L and C_L/C_D are inversely proportional to the trip height (excluding the $1\times\delta$ configuration). The configuration which obtains the highest lift-to-drag ratio is the $2\times\delta$ configuration. It obtains a lift-to-drag ratio that is almost five times that of the baseline case. The lowest performing configuration which still benefits the performance is the $6\times\delta$ trip height. It obtains a lift-to-drag ratio that is almost three times higher than the baseline case. To further understand the contributions of each component of the drag force, Table IV was created. Table IV displays the time-averaged pressure and friction drag percentages of each configuration for the AoA of 5°.

TABLE II. Simulation and mesh metrics for each configuration at the AoA of 5°.

Simulation	Elements	DOFs	Avg x^+_{equiv}	Avg y^+_{equiv}	Avg z^+_{equiv}	$\frac{\Delta x_{max}}{c}$	$\frac{\Delta y_{max}}{c}$	$\frac{\Delta z_{max}}{c}$
Baseline (p = 3)	165 000	10 560 000	10.3	0.6	16.7	0.03	0.01	0.03
$1\times\delta$ (p = 3)	174,750	11 184 000	8.8	0.7	17.3	0.03	0.01	0.03
$2\times\delta$ (p = 3)	174 750	11 184 000	9.4	0.6	17.5	0.03	0.01	0.03
$3\times\delta$ (p = 3)	174 750	11 184 000	9.0	0.6	16.7	0.03	0.01	0.03
$4\times\delta$ (p = 3)	174 750	11 184 000	9.2	0.6	16.7	0.03	0.01	0.03
$6\times\delta$ (p = 3)	174 750	11 184 000	8.6	0.6	15.9	0.03	0.01	0.03

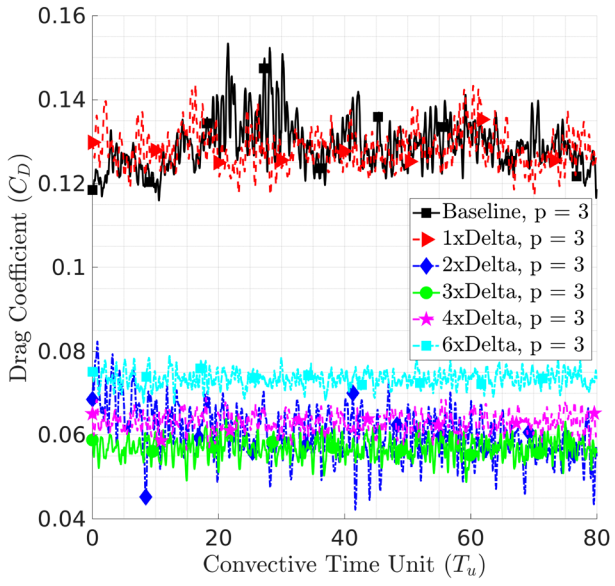

(a) Instantaneous drag coefficient

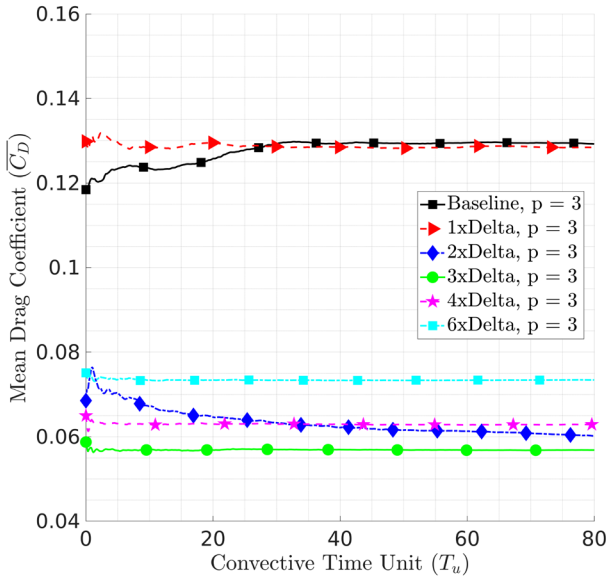

(b) Mean drag coefficient

FIG. 4. Time histories of drag coefficients for the AoA of 5°.

From Table IV, it can be seen that the pressure drag percentages follow a parabolic behavior with one local minimum and two local maxima. The maximum values are obtained by the $1 \times \delta$ and the $6 \times \delta$ configurations. For the friction drag percentages, it can be seen that the trend of this metric follows an inverted parabola with one local maximum and two local minima. The configuration which obtains the highest friction drag percentage is the $3 \times \delta$ configuration and the configurations which obtain the minimum values are the $1 \times \delta$ and $6 \times \delta$. The cause for both the pressure and friction drag percentages is easily identified when assessing Fig. 5. From Fig. 5(a), it is seen that the baseline and $1 \times \delta$ configurations display a primary LSB on the suction side of the airfoil which is significantly larger than the other configurations. Therefore, the pressure drag obtained by the baseline and $1 \times \delta$ configurations is due to the primary LSB. For the pressure drag obtained by the $6 \times \delta$ configuration, it is shown in Fig. 5(a) that this is attributed to it's large trip induced separation bubble (TISB). Although the $6 \times \delta$ configuration successfully reduces the primary LSB's size, its TISB is larger than the other configurations. This causes the elevated pressure drag shown in Table IV. For the friction drag, the $1 \times \delta$ configuration obtains the first of two local minima because its trip is ineffective at generating high-friction turbulent eddies. This is shown via Fig. 5(b). On the other hand, the ETT from the $6 \times \delta$ configuration successfully generates turbulent eddies which convect along the suction side of the airfoil's surface, contributing to elevated friction drag levels. However, as mentioned previously, the TISB from the $6 \times \delta$ configuration is excessively large and shifts the dominant contribution of drag toward pressure drag instead of friction drag.

Now that it has been shown that the tripped configurations (with the exception of the $1 \times \delta$ case) obtain a performance increase over the baseline case, the underlying physics of this performance increase will now be discussed. To begin, the turbulence generation effectiveness of each trip will be examined. Figure 5(a) displays the instantaneous iso-surfaces of Q-criteria colored by streamwise velocity for each configuration. It is easily observed that the behavior of the shear layer is significantly altered across the different configurations. The baseline case has a mostly two-dimensional, undisturbed, shear layer until just aft of the mid chord location where transition to turbulence occurs. This shear layer remains mostly the same for the $1 \times \delta$ case with the

TABLE III. Time-averaged aerodynamic coefficients and lift-to-drag ratio for the AoA of 5°.

Simulation	Lift coefficient	Drag coefficient	Lift-to-drag ratio
Baseline (p = 3)	0.678	0.129	5.239
$1 \times \delta$ (p = 3)	0.665	0.128	5.176
$2 \times \delta$ (p = 3)	1.403	0.060	23.553
$3 \times \delta$ (p = 3)	1.265	0.057	22.281
$4 \times \delta$ (p = 3)	1.208	0.063	19.224
$6 \times \delta$ (p = 3)	1.160	0.073	15.793

TABLE IV. Time-averaged pressure and friction drag percentages of each configuration for the AoA of 5°.

Simulation	Pressure drag (%)	Friction drag (%)
Baseline (p = 3)	90.7	9.3
$1 \times \delta$ (p = 3)	92.5	7.5
$2 \times \delta$ (p = 3)	84.5	15.5
$3 \times \delta$ (p = 3)	80.9	19.1
$4 \times \delta$ (p = 3)	81.6	18.4
$6 \times \delta$ (p = 3)	87.0	13.0

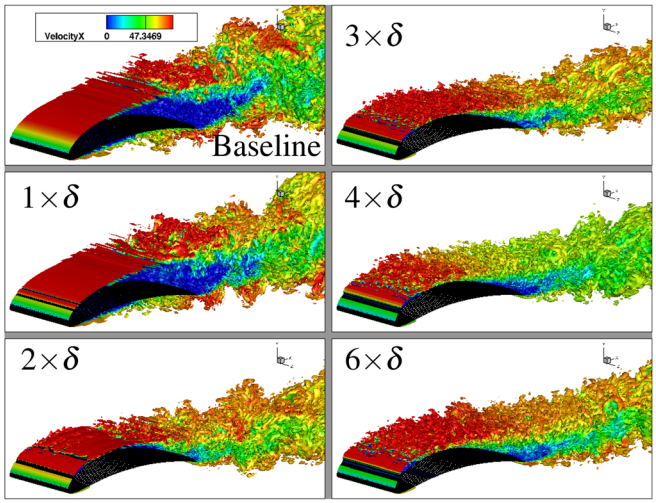

(a) Instantaneous iso-surfaces of Q-criteria for all configurations

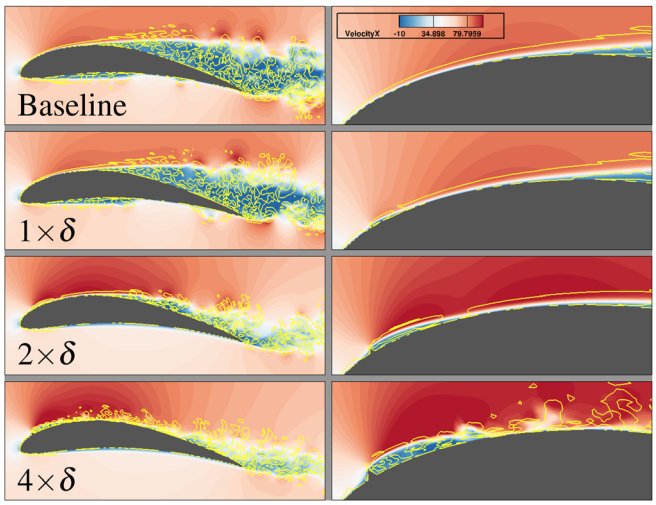

(b) Contours of instantaneous streamwise velocity with iso-lines of Q-criteria near the TISB at mid-span location.

FIG. 5. Turbulence characteristics at AoA of 5°.

exception of the small TISB generated by the trip. When progressing to the $2\times\delta$ case, strong three-dimensional variation in the shear layer occurs. This is shown as the streaks of turbulence on the right-hand side of the airfoil which are generated by the trip in Fig. 5(a). For the $2\times\delta$ case, it is also shown that the degree of separation is much smaller than any of the other configurations. When looking at the $3\times\delta$, $4\times\delta$, and $6\times\delta$ cases, it is shown that there is a proportional relationship between the trip height and turbulence level just aft of the trip. This proportional relationship between the trip height and turbulence generation is expected and means that of all of the tested configurations, the TISB of the $6\times\delta$ trip produces the largest levels of turbulent eddies. One final, interesting observation regarding Fig. 5(a) is that there is a sharp decay in streamwise velocity just aft of the mid-chord location for the $4\times\delta$ case that is not present in the $3\times\delta$ and $6\times\delta$ cases. This is shown as the sudden change from red to green on the colormap. To support the observations made when discussing Fig. 5(a), Fig. 5(b) was created. Figure 5(b) displays the contours of instantaneous streamwise velocity with iso-lines of Q-criteria near the trip's position at the mid-span location for the baseline, $1\times\delta$, $2\times\delta$, and $4\times\delta$ configurations. From Fig. 5(b), it becomes clear that the $1\times\delta$ configuration is able to generate a small TISB. However, the strength of its TISB is not strong enough to promote transition to turbulence. This is shown as the smooth iso-lines of yellow Q-criteria. As a result, the shear layer on the suction side of the airfoil remains nearly identical to that of the baseline case. From Fig. 5(b), it is shown that the shear layer for the $2\times\delta$ configuration also produced a visually noticeable TISB. However, the TISB at this spanwise location is not able to promote local transition, resulting in a shear layer thickness that is roughly the same as the baseline and $1\times\delta$ configuration at the mid-chord location. This observation, coupled with the observation from Fig. 5(a) that local pockets of transition are present on the right-hand side of the airfoil near the TISB for the $2\times\delta$ configuration, suggests that the $2\times\delta$ configuration is experiencing a bifurcation type phenomenon. This bifurcation causes some portions of the TISB from the $2\times\delta$ configuration to experience turbulent transition, whereas other portions of the airfoil's shear layer remain untripped. As a result of its TISB's inability to promote and sustain local transition at the mid-span location, the shear layer of the $2\times\delta$ configuration shown in Fig. 5(b) is similar to that of the baseline and $1\times\delta$ configurations. As was the case with the $1\times\delta$ and $2\times\delta$ configurations, the $4\times\delta$ configuration shown in Fig. 5(b) also displays a visually noticeable TISB. However, unlike the $1\times\delta$ and $2\times\delta$ configurations at the mid-span location, the TISB of the $4\times\delta$ configuration successfully promotes turbulent transition which is sustained along the suction side of the airfoil.

With a qualitative understanding of the turbulence levels of each TISB in place, the next step is to assess the impact of these turbulent structures on the downstream flow field. For this, contours of time-averaged turbulent kinetic energy (TKE) and streamwise flow velocity are shown via Fig. 6. From Fig. 6(a), it is easily seen that elevated levels of TKE are associated with the higher trip heights. This observation, coupled with the observations regarding Q-criteria, establishes that the trips induce turbulent eddies which then grow and elevate the TKE in the region where the TISB reattaches to the suction side of the airfoil. Because the TISB eventually reattaches to the suction side of the airfoil, it is critical to assess the TKE's influence on the behavior of the boundary layer near the separation location. To address this, Figs. 6(b) and 7 were generated. From Fig. 7, it can be seen that both laminar and turbulent boundary layers are present. The laminar profiles are obtained by the baseline, $1\times\delta$, and $2\times\delta$ configurations, whereas the turbulent profiles are obtained by the $3\times\delta$, $4\times\delta$, and $6\times\delta$ configurations. Of the laminar boundary layers, the baseline and $1\times\delta$ configurations obtain nearly identical laminar boundary layer profiles. This is in contrast to the $2\times\delta$ configuration which, even though it still obtains a laminar profile, is slightly closer to transitioning to a turbulent profile. For the turbulent profiles, it is shown that there is a clear proportionality between the trip height and the strength of turbulence obtained within the boundary layer. For example, the $3\times\delta$ configuration, although still turbulent, displays the weakest level of the turbulent profiles, whereas the $6\times\delta$ configuration shows the strongest turbulent profile. In addition to this relationship between trip height and

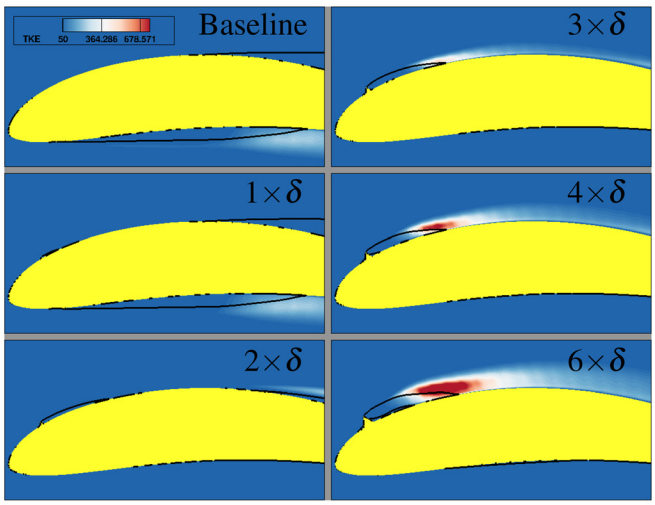

(a) Turbulent kinetic energy with TISB profile

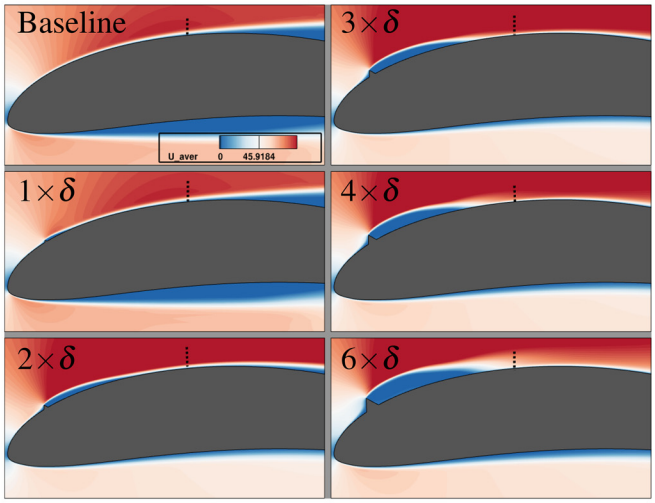

(b) Streamwise velocity with boundary layer locations

FIG. 6. Time-averaged contours for each configuration at mid-span location the AoA of 5°.

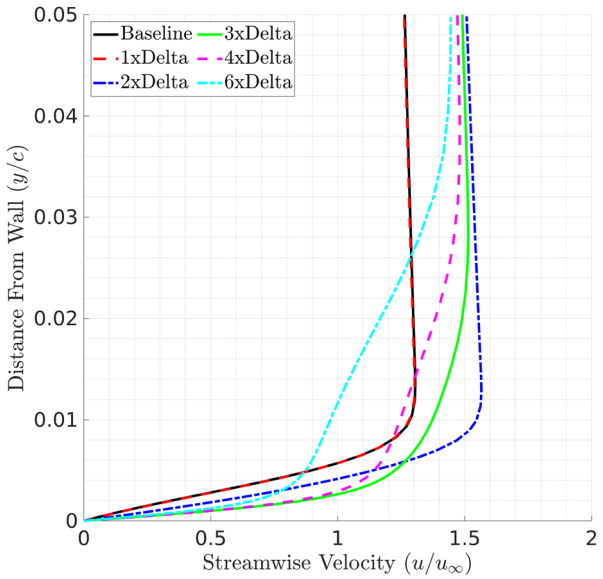

(a) Physical Units

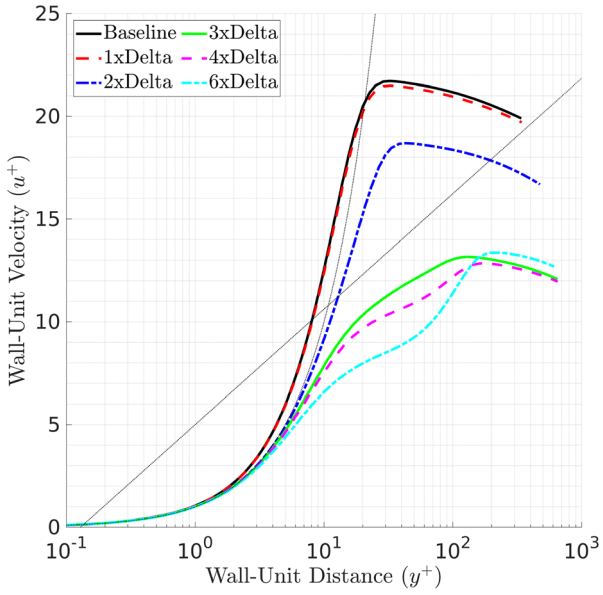

(b) Wall Units

FIG. 7. Time-averaged boundary layer profiles at the mid-span, quarter chord location for the AoA of 5°.

boundary layer turbulence, it is also clear that the boundary layer thickness at this location is inversely proportional to the trip height. This is seen most clearly in Fig. 7(a) when comparing the profile thicknesses of the $2\times\delta$ and $6\times\delta$ configurations. With this being said, it now becomes clear that the boundary layers of the trip heights greater than $1\times\delta$ are energized by the TKE generated by the turbulent eddies that are shed aft of the trip. This TKE injection strengthens the boundary layer and, in some instances, trips the boundary layer into turbulent (as is the case with $3\times\delta$, $4\times\delta$, and $6\times\delta$). With the behavior of the boundary layer established, the next step is to assess the impact of the boundary layer on the degree of separation over the suction side of the airfoil. Figure 8 shows the oilflow over the suction side of the airfoil at the AoA of 5°. The color map contours the streamwise skin friction coefficient. From Fig. 8, it is shown that the flow direction as well as the streamwise skin friction coefficient along the suction side of the airfoil for the baseline configuration is mostly two-dimensional until the point of separation. After the initial separation point, however, the flow direction becomes highly three-dimensional, whereas the streamwise skin friction coefficient remains mostly invariant in the spanwise direction. This behavior of high three-dimensional flow direction in regions of separated flow has also been mentioned in Refs. 55–57. A small reattachment point can be located just aft of the midchord

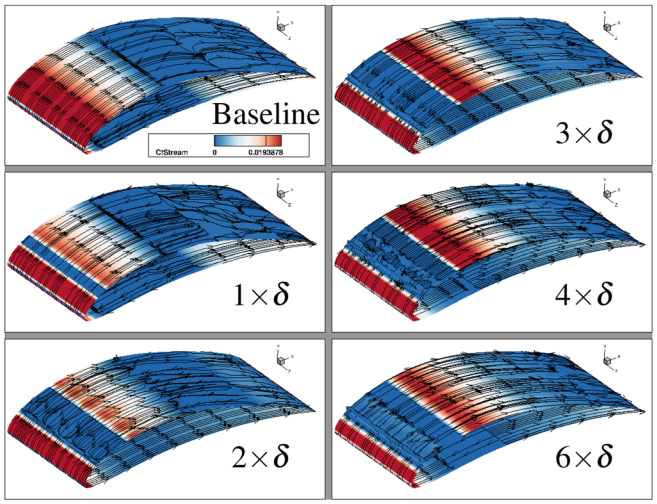

FIG. 8. Time-averaged oilflow for the AoA of 5°.

location. For the 1 ×δ configuration, the behavior of the flow direction and streamwise skin friction coefficient is similar to that of the baseline case. The only exception to this is the small pocket of separation just aft of the trip. As for the tripped configurations greater than 1 ×δ, it is shown that there is a mix between the dimensionality of the flow direction within the TISB. For example, the 2 ×δ and 4 ×δ configurations show strong three dimensionality, whereas the 3 ×δ and 6 ×δ configurations remain mostly two-dimensional within this region. One discernible trend which appears when analyzing the flow aft of the TISB reattachment is the proportional relationship between the trip height and the delay of the primary LSB separation point. For example, the 2 ×δ has a smaller delay in separation when compared to the 4 ×δ configuration whose separation is delayed almost until the trailing edge. This suggests that higher levels of TKE, which are generated by the trip and cause the boundary layers to strengthen, have a significant effect in delaying the separation. This ability of turbulent flows to resist separation has been published in various books[58,59] and directly supports the current explanation of how the ETTs improve the performance of the tested airfoil. One last observation regarding Fig. 8 is that almost all of the configurations (including the 1 ×δ and baseline case) show mainly two-dimensional behavior of the contours of streamwise skin friction coefficient. The only exception to this is the 2 ×δ configuration which show pockets of high skin friction coefficient which varies in the spanwise direction just aft of the TISB's reattachment point. To bring all of the previous observations back to the aspect of aerodynamic performance, the time-averaged pressure coefficient at the mid-span location for each airfoil configuration is shown in Fig. 9. From Fig. 9, it is shown that the flow along the suction side of the airfoil for the baseline configuration experiences a decrease in pressure coefficient within the region of $x/c = [0.0\ 0.2]$. After this region, however, the laminar flow along the suction side of the airfoil quickly loses its kinetic energy and separates, forming the primary LSB. This is shown in Fig. 9 as the pressure coefficient increasing in value then forming a pressure plateau which starts at $x/c = 0.35$. This behavior in pressure coefficient has been observed for a variety of airfoils which experience flow separation.[60–62] As for the tripped configurations, it is shown that

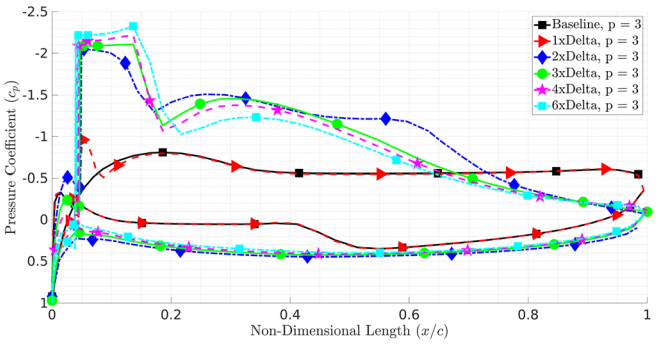

FIG. 9. Time-averaged pressure coefficient at the mid-span location for the AoA of 5°.

the 1 ×δ trip height is unable to alter the pressure profile of the airfoil, leading to nearly the same performance as the baseline case. On the other hand, all trip heights greater than 1 ×δ show a similar profile. On the suction side, these tripped profiles all start with a pressure drop followed by a small pressure plateau. This drop and plateau is caused by the TISB. Once the flow reattaches at roughly $x/c = 0.2$, the losses due to friction occur and begin to reduce the turbulent kinetic energy of the boundary layer. This is shown as the gradual increase in the pressure coefficient in Fig. 9 and was also shown explicitly in Fig. 6(a). Eventually, as was the case with the baseline configuration, the flow separates and the primary LSB is formed. However, due to the early accumulation of turbulent kinetic energy, the boundary layer of these tripped flows with a δ greater than one is able to remain attached to the suction surface much longer than the baseline and 1 ×δ case. This explains how the performance benefits shown previously were obtained. With regard to the pressure side, there is a noticeable separation bubble which occurs from $x/c = [0.0\ 0.4]$ on the baseline case. This pressure side LSB has also been noted in a previous work.[63] Similar to the suction side, the 1 ×δ configuration yields a nearly identical profile to the baseline case. On the other hand, all trip heights greater than 1 ×δ show a significant reduction in the size of the pressure side separation bubble. The causation of pressure side LSB reduction due to trip implementation will be discussed next.

Although the trip's ability to reduce the primary LSB magnitude is easily explained, the more subtle interaction is the relationship between the trip and the performance gain on the pressure side of the airfoil. The inclusion of the trip reduces and/or eliminates the pressure side LSB as was mentioned previously. Although this correlation was mentioned, the cause of this phenomenon was not explored until now. Figure 10 shows the time-averaged static pressure contours of the various tripped airfoils at the mid-span location. Additionally, streamtraces have been added to display flow direction. For the baseline and 1 ×δ trip configuration, it is easily seen that the stagnation point is located toward the suction side on the airfoil. On the other hand, the 2 ×δ, 3 ×δ, 4 ×δ, and 6 ×δ configurations have stagnation points that are shifted toward the pressure side of the airfoil. Additionally, the 2 ×δ, 3 ×δ, 4 ×δ, and 6 ×δ configurations exhibit an increased local AoA near the leading edge of the airfoil. This stagnation point shifting and increase in local AoA are the cause for the reduction in the size of the pressure side LSB. First, the stagnation shifting allows the flow near the stagnation point to traverse a shorter length before it reaches the

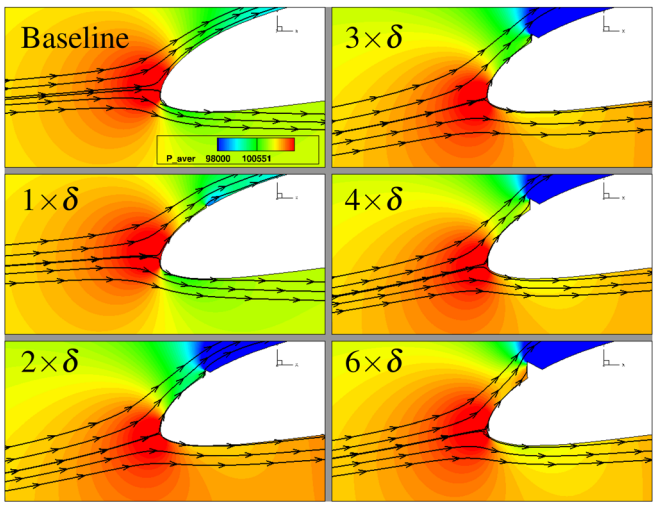

FIG. 10. Time-averaged pressure contour and streamtraces at leading edge location for the AoA of 5°.

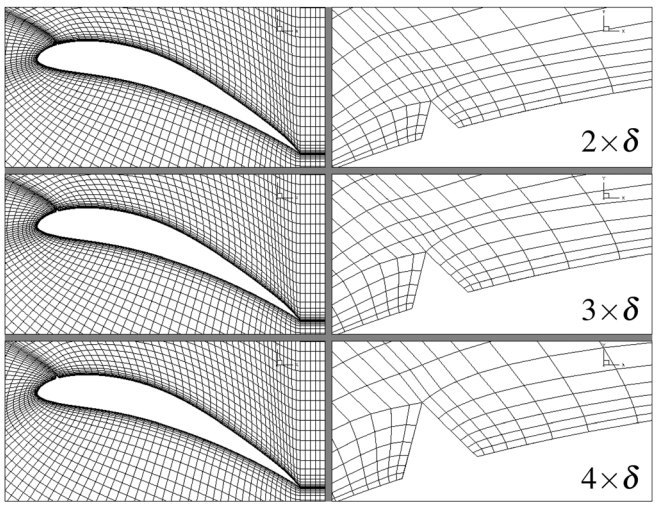

FIG. 11. Tripped E423 meshes for the AoA of 20°.

location of the pressure side LSB. This reduced traversal length lowers the amount of frictional losses experienced within the boundary layer and allows more kinetic energy to be retained to resist separation. Second, the increase in local AoA decreases the flow turning angle required to stay attached to the pressure side of the airfoil. This lower-turning-angle-less-separation phenomenon was explored for duct flows[64,65] and is best shown in Fig. 10 by comparing the baseline case to the $2\times\delta$ case. For the baseline case, we can see that the angle between the oncoming flow and the latter portion of the pressure side results in a turning angle that resembles a flow expansion. On the other hand, the angle between the oncoming flow and the latter portion of the pressure side of the $2\times\delta$ case results in a turning angle that resembles a flow compression. By changing the required flow turning angle from an expansion to a compression, the $2\times\delta$, $3\times\delta$, $4\times\delta$, and $6\times\delta$ configurations greatly reduce the flow separation and subsequently reduce and/or eliminate the pressure side LSB. When combining the observations made from this section, it becomes clear that the relative sizes of each of the three separation bubbles dictate the lift-to-drag ratio. For example, there is no drag penalty associated with a TISB for the baseline case. However, the drag penalty from the primary LSB for this configuration is substantial. On the other hand, the size of the primary LSB for the $6\times\delta$ configuration is minimal. However, the TISB for this configuration promotes too much separation, resulting in excessive drag in this region. With this being said, the configuration which best minimizes the drag incurred by all of the separation bubbles is the $2\times\delta$ configuration. At this AoA, its trip height is large enough to inject energy into the boundary layer without creating an excessively turbulent TISB and accruing unnecessary drag penalties.

B. AoA of 20°

Because it is imperative to also understand the performance of the trips in a near-stall condition, the $2\times\delta$, $3\times\delta$, and $6\times\delta$ configurations were also tested at an AoA of 20°. The mesh metrics for each simulation can be seen in Table V. The meshes at this angle of attack (Fig. 11) are just the rotated version of the meshes described in Sec. IV A. For the sake of brevity, the specifics of the mesh information are not repeated here. Identical to Sec. IV A, each of the configurations was sampled for eighty convective time units after reaching a quasi-steady state [see Eq. (2) for the definition of convective time unit]. To ensure no startup transience was present in the sampling period, the time history of lift-to-drag ratio is shown in Fig. 12. The C_L, C_D, and C_L/C_D for each configuration at the AoA of 20° are shown in Table VI. It is shown that none of the configurations are able to provide a benefit over the baseline case. Contrary to the findings in Sec. IV A, the trip height now as an inversely proportional relationship to the performance of the airfoil. The trip height which provides the lowest detriment is the $2\times\delta$ configuration which shows an increase in one

TABLE V. Simulation and mesh metrics for each configuration at the AoA of 20°.

Simulation	Elements	DOFs	Avg x^+_{equiv}	Avg y^+_{equiv}	Avg z^+_{equiv}	$\frac{\Delta x_{max}}{c}$	$\frac{\Delta y_{max}}{c}$	$\frac{\Delta z_{max}}{c}$
Baseline (p = 3)	165 000	10 560 000	9.8	0.7	16.6	0.03	0.01	0.03
$2\times\delta$ (p = 3)	174 750	11 184 000	9.4	0.7	16.8	0.03	0.01	0.03
$3\times\delta$ (p = 3)	174 750	11 184 000	8.9	0.6	15.9	0.03	0.01	0.03
$4\times\delta$ (p = 3)	174 750	11 184 000	7.5	0.5	14.0	0.03	0.01	0.03

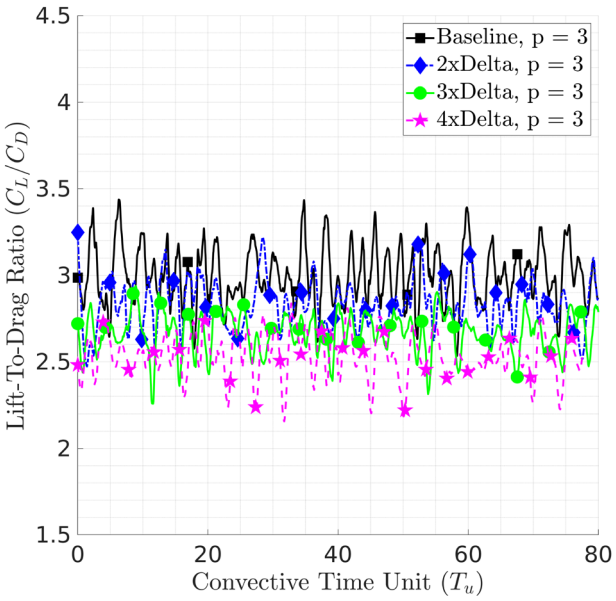

(a) Instantaneous lift-to-drag ratio

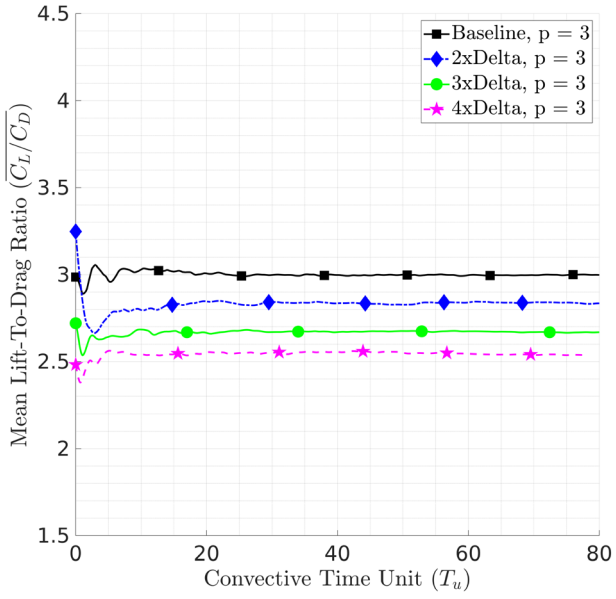

(b) Mean lift-to-drag ratio

FIG. 12. Time histories of lift-to-drag ratio for the AoA of 20°.

hundred and fifty drag counts. On the other hand, the tripped configuration which shows the lowest performance is the $4 \times \delta$ case which shows a lift-to-drag ratio reduction of approximately 15%. The performance deficit of the ETTs at a high AoA is expected and is consistent with other findings of passive flow control devices operating at off-design conditions.[66–68] As was performed previously for Sec. IV A, the time-averaged drag force was decoupled into pressure drag and friction drag. These drag components are shown in Table VII. From Table VII,

TABLE VI. Time-averaged aerodynamic coefficients and lift-to-drag ratio for the AoA of 20°.

Simulation	Lift coefficient	Drag coefficient	Lift-to-drag ratio
Baseline (p = 3)	1.334	0.445	3.001
$2 \times \delta$ (p = 3)	1.315	0.460	2.862
$3 \times \delta$ (p = 3)	1.302	0.487	2.674
$4 \times \delta$ (p = 3)	1.251	0.492	2.540

TABLE VII. Time-averaged pressure and friction drag percentages of each configuration for the AoA of 20°.

Simulation	Pressure drag (%)	Friction drag (%)
Baseline (p = 3)	97.8	2.2
$2 \times \delta$ (p = 3)	98.7	1.3
$3 \times \delta$ (p = 3)	98.5	1.5
$4 \times \delta$ (p = 3)	98.3	1.7

it is shown that the pressure drag for the tripped configurations is higher than the baseline case. As will be discussed further, this increase in pressure drag for the tripped configurations is due to the primary LSB encompassing the ETTs.

To understand the lack of performance enhancement at this angle of attack, a similar examination procedure to the one shown in Sec. IV A will be undertaken. More specifically, the turbulence generation due to the trips will be assessed via Q-criteria, followed by oilflows of the suction side of the airfoil. Next, the surface pressure coefficient and leading edge-stagnation point behavior will be assessed. The instantaneous iso-surfaces of Q-criteria colored by streamwise velocity are shown in Fig. 13(a). Similar to the observations found in Sec. IV A, it is shown that the level of turbulence generation is proportional to the height of the trip, whereas the length of the shear layer is inversely proportional to the trip size. One thing worth pointing out here is that the flow is clearly not able to reattach once passing over the trips, resulting in a very similar off-body flowfield to the baseline case. Because the Q-criteria for this angle of attack displays that the flow is not able to reattach aft of the trips, it is expected that the oilflows will also show very similar behavior between the different configurations. Figure 13(b) shows the oilflow over the suction side of the airfoil at the AoA of 20°. The color map contours the streamwise skin friction coefficient, whereas the black arrows depict the near-wall flow direction. From Fig. 13(b), it is shown that the streamwise skin friction coefficient along the suction side of the airfoil for every configuration is two dimensional. From this figure, it is easily seen that the trip is unable to alter the flow behavior along the suction side of the airfoil. As a result, the separation location is the same. Figure 14 shows the time-averaged pressure coefficient of the airfoil at the mid-span location for each configuration at the AoA of 20°. From Fig. 14, it is shown that the flow along both sides of the airfoil remains mostly the same regardless if the airfoil is tripped or not. The only exception to this is the behavior of the pressure along the suction side of the airfoil within the region of the leading edge. Within this region, it can be seen that there is a

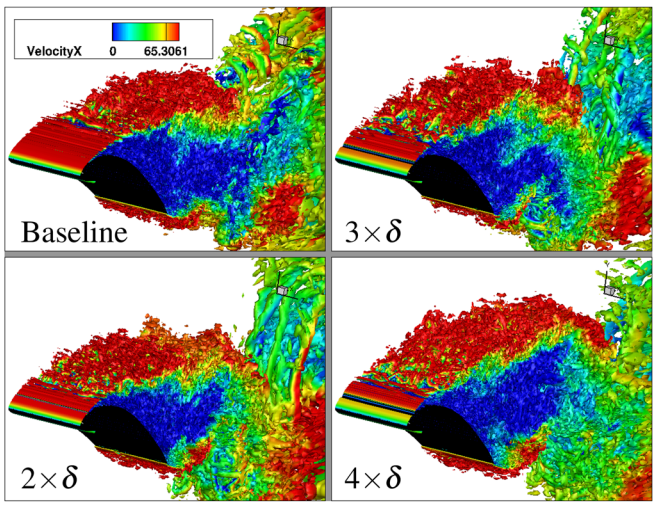

(a) Instantaneous Q-Criteria

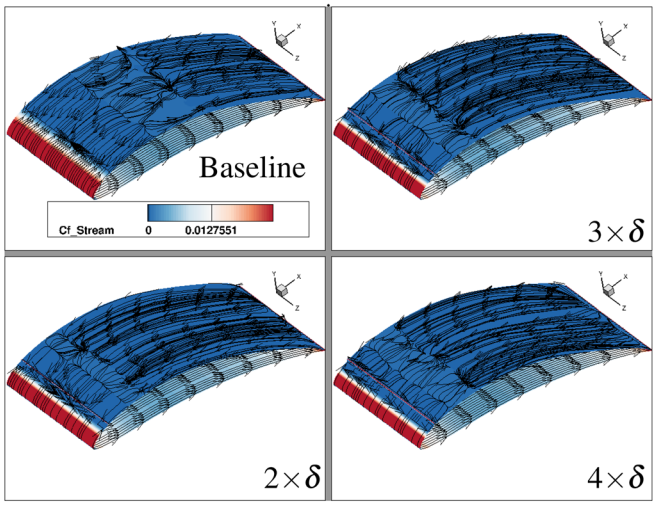

(b) Time averaged oil flow

FIG. 13. Q-criteria and oilflow for the AoA of 20°.

sudden pressure fluctuation which terminates at $x/c = 0.05$. At this point, a pressure decrease which looks like a step function is present for the tripped configurations. However, aft of $x/c = 0.05$, all configurations display a pressure plateau, indicating the presence of the primary LSB. To conclude this section on the AoA of 20°, the flowfield near the leading edge stagnation point will be assessed. Figure 15 shows the time-averaged pressure contour and flow direction of the airfoil at the leading edge, mid-span location for each configuration at the AoA of 20°. Unlike the results in Sec. IV A, no initial pressure side LSB is present. This is due to the airfoil operating at a high angle of attack. Another contrast to Sec. IV A is that instead of the ETTs shifting the stagnation point toward the pressure side of the airfoil, the trips now shift the stagnation point slightly toward the suction side of the airfoil. Additionally, instead of increasing the local flow angle near the leading

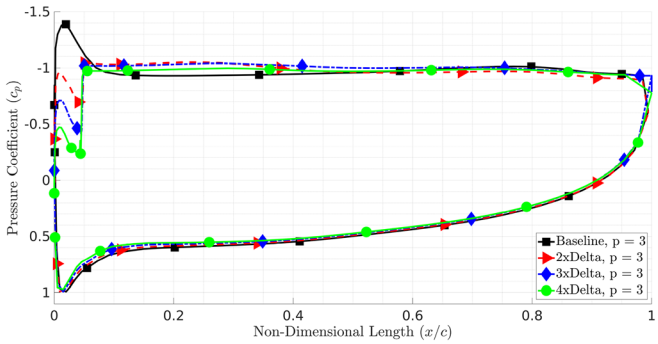

FIG. 14. Time-averaged pressure coefficient at the mid-span location for the AoA of 20°.

edge, the ETTs now create a shallower flow angle. This is most observable when comparing the flow angle between the baseline and $4 \times \delta$ configuration.

C. Comparison alongside existing designs from literature

Additional comparisons were carried out to assess the applicability of these ETTs as a suitable alternative to existing passive flow control methods. Figure 16(a) shows the tripped configurations from this study alongside several other passive flow control methods[25,26] which have been tested on the E423 airfoil at a Reynolds number of 40 000. The AoA of 5° results from this study are shown as the clustering of markers on the left-hand side of the figure. The results from the AoA of 20° are shown as the clustering on the top right. From Fig. 16(a), it is shown that the tripped configurations (with the exception of the $1 \times \delta$ case) show a substantial improvement over the existing designs for the low-drag regime. More specifically, for a drag coefficient of 0.05, the lift produced by the best ETT airfoil is nearly a factor of two higher than the best passive flow control design shown from the

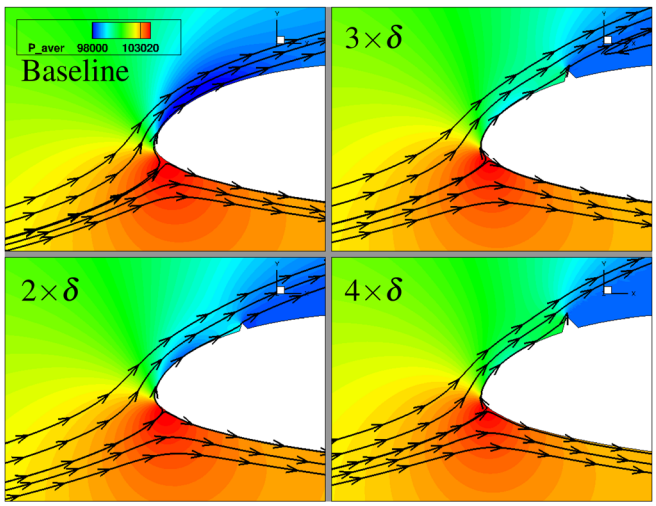

FIG. 15. Time-averaged pressure contour and streamtraces at the leading edge for the AoA of 20°.

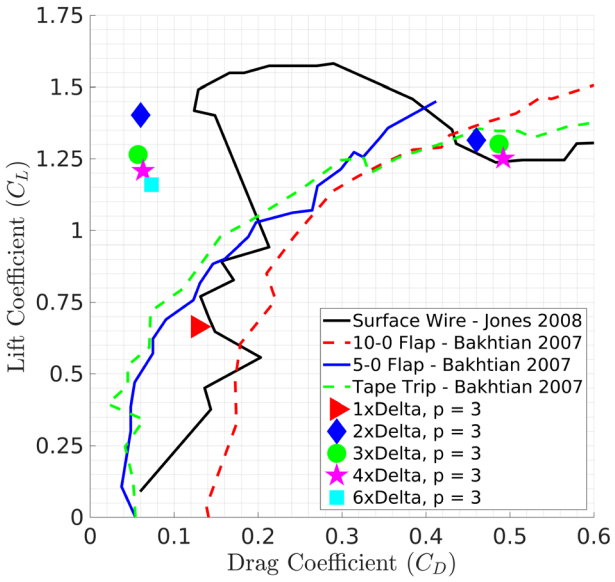

(a) Drag polar.

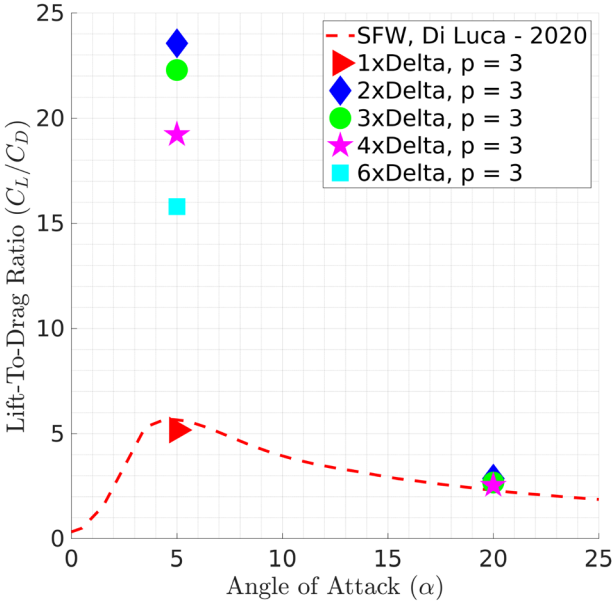

(b) Lift-to-drag ratio vs angle of attack.

FIG. 16. Comparisons to other passive flow control designs from literature for the E423 airfoil.

references. For the high-AoA-high-drag region on the right, it is shown that the ETT airfoils perform similar to that of existing designs. Figure 16(b) shows the lift-to-drag ratio of the tripped configurations from this study alongside the low-Reynold's number airfoil design called the SFW.[27] At the AoA of 5°, it is shown that the $1 \times \delta$ configuration performs nearly as well as the SFW. However, all tripped configurations with a trip height greater than $1 \times \delta$ show significant improvement over the SFW. The lowest performing ETT configuration (other than the $1 \times \delta$ case) is the $6 \times \delta$ configuration which obtains a factor of three improvement in the lift-to-drag ratio over the SFW. On the other hand, the best-performing ETT configuration at this AoA is the $2 \times \delta$ case which obtains nearly a factor of five improvement over the SFW. For the AoA of 20°, it is shown that all ETT configurations only marginally outperform the SFW.

Table VIII displays the ΔC_L, ΔC_D, and $\Delta(C_L/C_D)$ for the current set of tested E423 configurations at AoA of 5°. Additionally, Table VIII also displays the ΔC_L, ΔC_D, and $\Delta(C_L/C_D)$ for several other flow control designs from literature.[69,70] However, before discussing Table VIII, three things should be noted. First, the values of ΔC_L, ΔC_D, and $\Delta(C_L/C_D)$ are the percentage change of the C_L, C_D, and (C_L/C_D) with respect to the baseline airfoil for the same airfoil type. For example, the elliptic Canard-Rotor-Wing (CRW) airfoil with its plasma actuator off achieves a lift degradation of 1.9% when compared to the baseline elliptic CRW airfoil operating at a Reynold's number of 100 000, and an AoA of 5°. The second thing that should be kept in mind when assessing Table VIII, is that the baseline data (excluding the E423) is referenced from the corresponding literature.[69,70] In other words, the baseline Elliptic CRW and S8036 were not simulated using HpMusic. The last important factor which should be mentioned prior to discussing Table VIII is the difference in Reynold's numbers across the different airfoil types. When performing comparisons of flow control techniques, it is always better to assess configurations which operate at identical Reynold's numbers. However, because that route has already been exhausted with the previous comparisons within this manuscript, attempts were made to find other flow control techniques which were studied at Reynold's numbers similar to 40 000. With this being said, we can now assess Table VIII. First, we will compare the ETT configurations to the Elliptic CRW configurations.[69] From Table VIII, it is shown that the elliptic CRW configurations all display a degradation in lift when compared to the baseline elliptic CRW for the Reynold's number of 100 000. On the other hand, the E423 configurations with a trip height greater than $2 \times \delta$ significantly improve the lift coefficient relative to the baseline E423. This observations displays that in addition to being an effective passive flow control design, the ETTs show promise in outperforming more complex, active flow control approaches such as plasma actuators. Next, the effectiveness of the ETTs will be evaluated against another well-known passive flow control methodology, tape trips. From Table VIII, it is shown that the tape trips[69] at $Re_c = 75\,000$ display mixed results. For example, the trip locations of $x/c = 10\%$ and $x/c = 40\%$ display improvement regarding the lift coefficient but only the $x/c = 10\%$ and $x/c = 25\%$ configurations show improvement in (C_L/C_D). This is in contrast to the ETT configurations which show a strong, linear correlation between lift improvement and lift-to-drag ratio improvement. Additionally, the best-performing tape trip at $Re_c = 75\,000$ obtains a lift-to-drag ratio improvement of 8.6% over its baseline configuration, whereas the highest performing ETT setup outperforms its baseline configuration by 349.6%. These two observations show that in addition to having a more predictable performance envelope, the ETTs may be able to outperform tape trips in terms of performance improvement. The last comparison that will be carried out using Table VIII is the comparison between the ETT configurations and the tape trips at $Re_c = 100\,000$. For the tape trips, it is now observable that all three configurations show an increase in C_L, a decrease in C_D, and an increase in (C_L/C_D) relative to the baseline S8036. Of the three configurations at this

TABLE VIII. Lift and drag improvements for AoA of 5° compared to other flow control designs from literature at similar Reynold's numbers.

Airfoil type	Configuration	Re_c	$\Delta C_L(\%)$	$\Delta C_D(\%)$	$\Delta(C_L/C_D)(\%)$
E423	$1\times\delta$ (p = 3)	40 000	−1.9	−0.8	−1.2
E423	$2\times\delta$ (p = 3)	40 000	106.9	−53.5	349.6
E423	$3\times\delta$ (p = 3)	40 000	85.6	−55.8	325.3
E423	$4\times\delta$ (p = 3)	40 000	78.2	−51.2	266.9
E423	$6\times\delta$ (p = 3)	40 000	71.1	−43.4	201.5
Elliptic CRW	Plasma actuator off[69]	100 000	−1.9	N/A	N/A
Elliptic CRW	Plasma actuator on (Steady)[69]	100 000	−8.5	N/A	N/A
Elliptic CRW	Plasma actuator on (Duty cycle)[69]	100 000	−19.7	N/A	N/A
S8036	Tape trip,[70] $\frac{h}{c}=0.1\%$, $\frac{x}{c}=10\%$	75 000	0.3	−5.7	6.4
S8036	Tape trip,[70] $\frac{h}{c}=0.1\%$, $\frac{x}{c}=25\%$	75 000	−9.5	−16.9	8.6
S8036	Tape trip,[70] $\frac{h}{c}=0.1\%$, $\frac{x}{c}=40\%$	75 000	3.6	7.0	−3.6
S8036	Tape trip,[70] $\frac{h}{c}=0.1\%$, $\frac{x}{c}=10\%$	100 000	0.6	−3.8	4.6
S8036	Tape trip,[70] $\frac{h}{c}=0.1\%$, $\frac{x}{c}=25\%$	100 000	1.2	−29.9	44.4
S8036	Tape trip,[70] $\frac{h}{c}=0.1\%$, $\frac{x}{c}=40\%$	100 000	7.3	−10.5	19.9

Reynold's number, the trip location of $\frac{x}{c}=25\%$ displays the highest lift-to-drag ratio improvement with a value of 44.4%. However, none of the three tape trips at this Reynold's number obtains the same performance increase as the ETTs for any of the tested performance parameters. This, along with the previous observations when discussing Table VIII, suggests that ETTs may significantly outperform well-established flow control methodologies in terms of airfoil performance enhancement.

V. CONCLUSIONS

A new passive flow control technique was developed and tested for the Eppler E423 airfoil at a Reynolds number based on chord of 40 000. The design was first tested against an unmodified/baseline E423 via wall-resolved large eddy simulation (WRLES) at angles of attack of 5° and 20°. Metrics such as lift-to-drag ratio, pressure coefficient profiles, oilflow, iso-surfaces of Q-criteria, and leading edge flow behavior were compared. It was shown that the ETTs with a trip height greater than $1\times\delta$ were successful in eliminating both the suction side and pressure side separation bubbles at $\alpha = 5°$, a phenomenon which has not yet been seen before for the E423 operating in MAV-scale conditions. After showing substantial improvements in lift-to-drag ratio over the baseline case for the AoA of 5°, the ETT study was replicated for the AoA of 20° to see if the results would hold in a near-stall configuration. At this AoA, it was shown that the trips were unable to prevent and/or delay the onset of the primary LSB. Comparisons against existing passive flow control techniques from the literature via drag polar were then carried out. The included reference techniques included wire trips, tape trips, and leading edge flaps. It was shown that the ETTs produced more lift than existing passive flow control designs by almost a factor of two in the low-drag regime and performed similar to existing designs in the high-drag regime. Of the tested trip heights, the $2\times\delta$ configuration displayed the largest improvement in aerodynamic performance over the baseline case. Its TISB is large enough to energize the boundary layer which reduces flow separation without accruing unnecessary drag penalties. As a result, this configuration is able to minimize the drag incurred by both the LSB and TISB. Comparisons of lift-to-drag ratio alongside a in particular, designed wing called the SFW was also conducted. It was shown that the ETTs outperformed the SFW in terms of lift-to-drag ratio at the AoAs of 5° and 20°. Although the ETTs performed marginally better than the SFW at an AoA of 20°, the performance benefit of using ETTs over the SFW at an AoA of 5° is almost a factor of five. Finally, the performance benefit of the ETTs was assessed alongside several well-established flow control methodologies such as plasma actuators and tape trips. It was shown that the ETTs provided superior results in terms of lift enhancement, drag reduction, and lift-to-drag ratio improvement. These results indicate that ETTs show promise in outperforming both active and passive flow control designs.

VI. FUTURE WORK

The current work presented a novel passive flow control device called the ETT. In addition, the document presents a series of six difference configurations tested at a Reynold's number based on chord of 40 000. These six airfoil configurations were tested at 5° and 20° angles of attack. Although this is a solid foundation to begin our understanding of the performance and mechanics of these ETTs, several suggestions for follow-on work are listed. First, is the optimal location of the ETT. Second is the influence of freestream turbulence intensity (FSTI) on the performance aspect of the ETTs. According to previous studies,[71–73] increasing the turbulence intensity will reduce the size and strength of the primary LSB, thus increasing the baseline airfoil's performance and reducing the need for flow control. Third is the

effectiveness of the ETTs at different angles of attack. Some previous work displays that the lift coefficient of low-Reynold's number airfoils remains mostly linear for angles of attack smaller than the stall angle.[69,70,74] This suggests that the beneficial results shown for the ETTs at $\alpha = 5^\circ$ will hold for nearby angles such as $\alpha = 4^\circ$ and $\alpha = 6^\circ$. However, when approaching the stall angle, the lift coefficient and other performance parameters become non-linear. This means that the results for $\alpha = 20^\circ$ shown in this manuscript may not be similar for nearby angles of attack.

ACKNOWLEDGMENTS

This work was performed at the HPC facilities operated by the Center for Research Computing at the University of Kansas supported, in part, through the National Science Foundation MRI Award No. 2117449. This material is based upon work supported by the Air Force Office of Scientific Research under Award No. FA9550-20-1-0315 and Army Research Office under Award No. W911NF-20-1-0065.

AUTHOR DECLARATIONS

Conflict of Interest

The authors have no conflicts to disclose.

Author Contributions

Salman Rahmani: Conceptualization (equal); Data curation (equal); Formal analysis (equal); Funding acquisition (equal); Investigation (equal); Methodology (equal); Project administration (equal); Resources (equal); Software (equal); Supervision (equal); Validation (equal); Visualization (equal); Writing – original draft (equal); Writing – review & editing (equal). **Zhi Jian Wang:** Conceptualization (equal); Data curation (equal); Formal analysis (equal); Funding acquisition (equal); Investigation (equal); Methodology (equal); Project administration (equal); Resources (equal); Software (equal); Supervision (equal); Validation (equal); Visualization (equal); Writing – original draft (equal); Writing – review & editing (equal).

DATA AVAILABILITY

The data that support the findings of this study are available from the corresponding author upon reasonable request.

REFERENCES

[1]S. Hwan Song, H. Wook Shon, G. Yang Yeon, and H. Ryeol Choi, "Design and implementation of cloud-like soft drone s-cloud," in *2018 IEEE/RSJ International Conference on Intelligent Robots and Systems (IROS)* (IEEE, 2018), pp. 1–9.

[2]K. Valavanis, *Advances in Unmanned Aerial Vehicles: State of the Art and the Road to Autonomy* (Springer Dordrecht, 2007).

[3]K. Hasan, S. Newaz, and M. S. Ahsan, "Design and development of an aircraft type portable drone for surveillance and disaster management," Int. J. Intell. Unmanned Syst. **6**, 147–159 (2018).

[4]G. Cai, K.-Y. Lum, B. M. Chen, and T. H. Lee, "A brief overview on miniature fixed-wing unmanned aerial vehicles," in *IEEE ICCA 2010* (IEEE, 2010), pp. 285–290.

[5]C. Cuerno Rejado, L. Garcia Hernandez, A. Sanchez Carmona, A. Carrió Fernández, J. L. Sanchez Lopez, and P. Campoy Cervera, "Evolución histórica de los vehículos aéreos no tripulados hasta la actualidad," Dyna **91**, 282–288 (2016).

[6]B. Kinzig, "Global Hawk systems engineering: Case study," Technical Report No. 8844 (Defense Technical Information Center, Fort Belvoir, 2010).

[7]H. Qin, J. Q. Cui, J. Li, Y. Bi, M. Lan, M. Shan, W. Liu, K. Wang, F. Lin, Y. F. Zhang, and B. M. Chen, "Design and implementation of an unmanned aerial vehicle for autonomous firefighting missions," in *2016 12th IEEE International Conference on Control and Automation (ICCA)* (IEEE, 2016), pp. 62–67.

[8]K. Nonami, "Research and development of drone and roadmap to evolution," J. Rob. Mechatron. **30**, 322–336 (2018).

[9]V. Be, F. Adam, and I., Jr, "Unmanned combat air vehicle: Mq-9 reaper," in International Conference of Scientific Paper AFASES 2014 (2014).

[10]N. Mahamud, G. M. Shahriar, H. U. Khan, S. Sharmin, and N. J. Lisa, "ALW drone: A new design and efficient approach," in *2016 19th International Conference on Computer and Information Technology (ICCIT)* (IEEE, 2016), pp. 474–479.

[11]B. Loxton, M. Abdulrahim, and S. Watkins, "An investigation of fixed and rotary wing mav flight in replicated atmospheric turbulence," AIAA Paper No. 2008-227, 2008.

[12]S. Watkins, J. Milbank, B. J. Loxton, and W. H. Melbourne, "Atmospheric winds and their implications for microair vehicles," AIAA J. **44**, 2591–2600 (2006).

[13]P. Ifju, D. Jenkins, S. Ettinger, Y. Lian, W. Shyy, and M. Waszak, "Flexible-wing-based micro air vehicles," AIAA Paper No. 2002-705, 2002.

[14]*Active Flow Control: Papers Contributed to the Conference "Active Flow Control 2006", Berlin, Germany, September 27 to 29, 2006* 95, edited by R. King (Springer, Berlin, New York, 2007).

[15]A. Mohamed, S. Watkins, R. Clothier, M. Abdulrahim, K. Massey, and R. Sabatini, "Fixed-wing MAV attitude stability in atmospheric turbulence–part 2: Investigating biologically-inspired sensors," Prog. Aerosp. Sci. **71**, 1–13 (2014).

[16]A. Panta, "Qualitative investigation of the dynamics of a leading edge control surfaces for MAV applications," in International Micro Air Vehicle Conference and Flight Competition (IMAV) 2017 (2017).

[17]K. Rengasamy and A. C. Mandal, "Experiments on effective tripping device in a zero pressure gradient turbulent boundary layer," J. Phys.: Conf. Ser. **822**, 012016 (2017).

[18]B. K. Sreejith and S. Alangar, "Numerical study on effect of boundary layer trips on aerodynamic performance of E216 airfoil," Eng. Sci. Technol. Int. J. **21**, 77 (2018).

[19]B. K. Sreejith, "Effect of boundary layer trip and tubercles on aerodynamic performance of E216 airfoil," Ph.D. thesis (National Institute of Technology Karnataka, 2018).

[20]B. K. Sreejith, A. Sathyabhama, and S. S. Kumar, "Comparative study on the aerodynamic performance of airfoil with boundary layer trip of various geometrical shapes," J. Phys.: Conf. Ser. **1854**, 012003 (2021).

[21]X. Li, K. Yang, and X. Wang, "Experimental and numerical analysis of the effect of vortex generator height on vortex characteristics and airfoil aerodynamic performance," Energies **12**, 959 (2019).

[22]A. Seshagiri, E. Cooper, and L. W. Traub, "Effects of vortex generators on an airfoil at low REYNOLDS numbers," J. Aircr. **46**, 116–122 (2009).

[23]A. Haines, "Airfoil design and data. R. Eppler. Springer-Verlag, Heidelberger Platz 3, D-1000 Berlin 33, Germany. 1990. 562 pp. Illustrated. DM128,00," Aeronaut. J. **95**, 289–289 (1991).

[24]A. Altman and G. Allemand, "Post-stall performance improvement through bio-inspired passive covert feathers," AIAA Paper No. 2016-2042, 2016.

[25]N. Bakhtian, H. Babinsky, A. Thomas, and G. Taylor, "The low Reynolds number aerodynamics of leading edge flaps," AIAA Paper No. 2007-662, 2007.

[26]A. R. Jones, N. M. Bakhtian, and H. Babinsky, "Low Reynolds number aerodynamics of leading-edge flaps," J. Aircr. **45**, 342–345 (2008).

[27]M. D. Luca, S. Mintchev, Y. Su, E. Shaw, and K. Breuer, "A bioinspired separated flow wing provides turbulence resilience and aerodynamic efficiency for miniature drones," Sci. Rob. **5**, eaay8533 (2020).

[28]M. D. Luca, "The use of separation induced laminar to turbulent flow transition to improve the performance and robustness of low Reynolds numbers airfoils and wings," Ph.D. thesis (Brown University, 2013).

[29]L. Wang, L.-H. Feng, Y. Liang, Y.-L. Chen, and Z.-Y. Li, "Vortex control strategy for unsteady aerodynamic optimization of a plunging airfoil at a low Reynolds number," Phys. Fluids **33**, 117110 (2021).

[30]S. Kasmaiee, M. Tadjfar, and S. Kasmaiee, "Machine learning-based optimization of a pitching airfoil performance in dynamic stall conditions using a suction controller," Phys. Fluids **35**, 095121 (2023).
[31]C. Hirsch, *Numerical Computation of Internal and External Flows: The Fundamentals of Computational Fluid Dynamics* (Elsevier, 2007).
[32]Z. Wang, Y. Li, F. Jia, G. Laskowski, J. Kopriva, U. Paliath, and R. Bhaskaran, "Towards industrial large eddy simulation using the FR/CPR method," in *Ninth International Conference on Computational Fluid Dynamics (ICCFD9), 2017* [Comput. Fluids **156**, 579–589 (2017)].
[33]H. T. Huynh, "A flux reconstruction approach to high-order schemes including discontinuous Galerkin methods," AIAA Paper No. 2007-4079, 2007.
[34]T. Haga, H. Gao, and Z. J. Wang, "A high-order unifying discontinuous formulation for the Navier–Stokes equations on 3D mixed grids," Math. Modell. Nat. Phenom. **6**, 28–56 (2011).
[35]Z. Wang and H. Gao, "A unifying lifting collocation penalty formulation including the discontinuous Galerkin, spectral volume/difference methods for conservation laws on mixed grids," J. Comput. Phys. **228**, 8161–8186 (2009).
[36]E. J. de Araujo, J. Filho, and Z. J. Wang, "Efficient implementation of the FR/CPR method on GPU clusters for industrial large eddy simulation," AIAA Paper No. 2020-3031, 2020.
[37]M. A. Alhawwary and Z. J. Wang, "Implementation of a FWH approach in a high-order les tool for aeroacoustic noise predictions," AIAA Paper No. 2020-1724, 2020.
[38]H. Huynh, Z. Wang, and P. Vincent, "High-order methods for computational fluid dynamics: A brief review of compact differential formulations on unstructured grids," in *12th USNCCM mini-symposium of High-Order Methods for Computational Fluid Dynamics - A special issue dedicated to the 80th birthday of Professor Antony Jameson, 2014* [Comput. Fluids **98**, 209–220 (2014)].
[39]Z. J. Wang, "High-order computational fluid dynamics tools for aircraft design," Philos. Trans. R. Soc. A: Math., Phys. Eng. Sci. **372**, 20130318 (2014).
[40]B. Cockburn, G. E. Karniadakis, and C.-W. Shu, *Discontinuous Galerkin Methods: Theory, Computation and Applications* (Springer Berlin, Heidelberg, 2000).
[41]Y. Liu, M. Vinokur, and Z. J. Wang, "Discontinuous spectral difference method for conservation laws on unstructured grids," in *Computational Fluid Dynamics 2004*, edited by C. Groth and D. W. Zingg (Springer Berlin Heidelberg, Berlin, Heidelberg, 2006), pp. 449–454.
[42]F. Bassi and S. Rebay, "A high order discontinuous Galerkin method for compressible turbulent flows," in *Discontinuous Galerkin Methods*, edited by B. Cockburn, G. E. Karniadakis, and C.-W. Shu (Springer Berlin Heidelberg, Berlin, Heidelberg, 2000), pp. 77–88.
[43]Y. Li and Z. J. Wang, "A convergent and accuracy preserving limiter for the FR/CPR method," AIAA Paper No. 2017-0756, 2017.
[44]V. Vatsa, M. Carpenter, and D. Lockard, "Re-evaluation of an optimized second order backward difference (BDF2OPT) scheme for unsteady flow applications," AIAA Paper No. 2010-122, 2012.
[45]S. Yoon and A. Jameson, "Lower-upper symmetric-Gauss-Seidel method for the Euler and Navier–Stokes equations," AIAA J. **26**, 1025–1026 (1988).
[46]F. Jia, Z. Wang, R. Bhaskaran, U. Paliath, and G. M. Laskowski, "Accuracy, efficiency and scalability of explicit and implicit FR/CPR schemes in large eddy simulation," Comput. Fluids **195**, 104316 (2019).
[47]A. Aihara and S. Kawai, "Effects of spanwise domain size on les-predicted aerodynamics of stalled airfoil," AIAA J. **61**, 1440–1446 (2023).
[48]J. M. Turner and J.-W. Kim, "Numerical investigation into the effect of separation and stall on aerofoil noise," in Proceedings of the 11th International Symposium on Turbulence and Shear Flow Phenomena (TSFP-11) (2019).
[49]S. Moreau, J. Christophe, and M. Roger, "LES of the trailing-edge flow and noise of a NACA0012 airfoil near stall," in *Proceedings of the Summer Program* (Stanford University, Center for Turbulence Research Stanford, 2008), pp. 317–329.
[50]D. Luo, D. Huang, and X. Sun, "Passive flow control of a stalled airfoil using a microcylinder," J. Wind Eng. Ind. Aerodyn. **170**, 256–273 (2017).
[51]X. Shi, S. Xu, L. Ding, and D. Huang, "Passive flow control of a stalled airfoil using an oscillating micro-cylinder," Comput. Fluids **178**, 152–165 (2019).
[52]W. Mostafa, A. Abdelsamie, M. Mohamed, D. Thévenin, and M. Sedrak, "Aerodynamic performance improvement using a micro-cylinder as a passive flow control around the s809 airfoil," IOP Conf. Ser.: Mater. Sci. Eng. **973**, 012040 (2020).
[53]M. S. P. Spalart, L. Hedges, and A. Travin, "Simulation of active flow control on a stalled airfoil," Flow, Turbul. Combust. **71**, 361 (2003).
[54]S. Dahlström and L. Davidson, "Large eddy simulation applied to a high-Reynolds flow around an airfoil close to stall," AIAA Paper No. 2003-776, 2003.
[55]M. Genc and U. Kaynak, "Control of laminar separation bubble over a NACA2415 aerofoil at low re transitional flow using blowing/suction," Int. Conf. Aerosp. Sci. Aviat. Technol. **13**, 1–17 (2009).
[56]G. Schewe, "Reynolds-number effects in flow around more-or-less bluff bodies," J. Wind Eng. Ind. Aerodyn. **89**, 1267–1289 (2001).
[57]Z. J. Wang, "Wall-modeled large eddy simulation of the NASA CRM high-lift configuration with the high-order FR/CPR method," AIAA Paper No. 2022-3395, 2022.
[58]P. K. Chang, "Steady separation of incompressible laminar flow from two-dimensional surfaces," in *Separation of Flow*, edited by P. K. Chang (Pergamon, 1970), Chap. II, pp. 55–95.
[59]M. Gad-el Hak and D. M. Bushnell, "Separation control," J. Fluids Eng. **113**, 5 (1991).
[60]S. Eisenbach and R. Friedrich, "Large-eddy simulation of flow separation on an airfoil at a high angle of attack and Re = 105 using cartesian grids," Theor. Comput. Fluid Dyn. **22**, 213 (2008).
[61]M. Xiao, Y. Zhang, and H. Chen, "Numerical study of an iced airfoil using window-embedded rans/les hybrid method," AIAA Paper No. 2017-3761, 2017.
[62]J. H. Almutairi, L. E. Jones, and N. D. Sandham, "Intermittent bursting of a laminar separation bubble on an airfoil," AIAA J. **48**, 414–426 (2010).
[63]S. K. Rahmani and Z. J. Wang, "Computational study of passive flow control for a MAV-scale Eppler E423 airfoil," AIAA Paper No. 2023-0054, 2023.
[64]Y. Khong, N. Nordin, S. Seri, A. Mohammed, A. Sapit, I. Taib, K. Abdullah, A. Sadikin, and M. Razali, "Effect of turning angle on performance of 2-D turning diffuser via asymptotic computational fluid dynamics," IOP Conf. Ser.: Mater. Sci. Eng. **243**, 012013 (2017).
[65]T. Xian, N. Nordin, A. Hariri, N. Nasir, N. Mat Isa, M. Yahya, and S. Md Seri, "Asymptotic computational fluid dynamic (ACFD) study of three-dimensional turning diffuser performance by varying angle of turn," Int. J. Integr. Eng. **11**, 109–118 (2019).
[66]O. M. Fouatih, M. Medale, O. Imine, and B. Imine, "Design optimization of the aerodynamic passive flow control on NACA 4415 airfoil using vortex generators," Eur. J. Mech. B **56**, 82–96 (2016).
[67]A. Aboelezz, H. Ghali, G. Elbayomi, and M. Madboli, "A novel VAWT passive flow control numerical and experimental investigations: Guided vane airfoil wind turbine," Ocean Eng. **257**, 111704 (2022).
[68]S. Chowdhury and V. Maldonado, "Bio-inspired active and passive surface flow control for aerodynamic efficiency," AIAA Paper No. 2017-4120, 2017.
[69]X. Meng, H. Hu, X. Yan, F. Liu, and S. Luo, "Lift improvements using duty-cycled plasma actuation at low Reynolds numbers," Aerosp. Sci. Technol. **72**, 123–133 (2018).
[70]L. W. Traub, "Experimental investigation of the effect of trip strips at low Reynolds number," J. Aircr. **48**, 1776–1784 (2011).
[71]S. Ravi, S. Watkins, J. Watmuff, K. Massey, P. Peterson, and M. Marino, "Influence of large-scale freestream turbulence on the performance of a thin airfoil," AIAA J. **50**, 2448–2459 (2012).
[72]J. Michálek, M. Monaldi, and T. Arts, "Aerodynamic performance of a very high lift low pressure turbine airfoil (T106C) at low Reynolds and high Mach number with effect of free stream turbulence intensity," J. Turbomach. **134**, 061009 (2012).
[73]R. F. Huang and H. W. Lee, "Effects of freestream turbulence on wing-surface flow and aerodynamic performance," J. Aircr. **36**, 965–972 (1999).
[74]H. Hu and Z. Yang, "An experimental study of the laminar flow separation on a low-Reynolds-number airfoil," J. Fluids Eng. **130**, 051101 (2008).